Imaging Shallow Complex V_s Structure Using F–J Surface-Wave Tomography with Partition Similarity Test: A Case Study at the San Jacinto Fault Zone

Shuhao Song[1], Zhengbo Li[1,2,3], Juqing Chen[1], Fengjiang Ju[1], Chunquan Yu[1,2,3], and Xiaofei Chen*[1,2,3]

Abstract

Dense seismometer arrays offer new opportunities for refining the exploration of near-surface near-fault structures. By deploying regional dense seismic arrays, seismologists have significantly advanced their insights into structures, rupture processes, and dynamic behaviors for fault systems. However, achieving high-resolution shear-wave velocity structures remains challenging. This study applies the frequency–Bessel transform (F-J) method, a multimodal surface-wave tomography technique, to image complex subsurface systems. The F-J method enables broad frequency band dispersion curves, overtone extraction, and improved resolution. To address challenges in reliable subarray selection for 3D complex subsurface imaging when using this array-based method, we introduce a partition similarity test to quantitatively and adaptively generate suitable subarrays. We apply this method to image the Sagebrush flat site along the Clark fault branches of the San Jacinto fault zone, demonstrating its effectiveness in mitigating the branched dispersion phenomenon that appears in the traditional workflow of the F-J method. The high-resolution imaging results reveal two low-velocity anomalies, a trapping structure, an inferred fault, and significant lateral velocity variations along the Clark fault branches.

Cite this article as Song, S., Z. Li, J. Chen, F. Ju, C. Yu, and X. Chen (2025). Imaging Shallow Complex V_s Structure Using F–J Surface-Wave Tomography with Partition Similarity Test: A Case Study at the San Jacinto Fault Zone, *Seismol. Res. Lett.* **XX**, 1–15, doi: 10.1785/0220240465.

Supplemental Material

Introduction

In the past decade, ambient noise data has been recorded by many regional dense arrays consisting of portable short-period seismometers to explore refined structures (Ben-Zion *et al.*, 2015; Hansen and Schmandt, 2015; Nakata *et al.*, 2015; Chang *et al.*, 2016; Wei *et al.*, 2018). Surface-wave dispersion is an essential observation to constrain velocity structure (Trampert and Woodhouse, 1995; Shapiro and Ritzwoller, 2002; Shapiro *et al.*, 2005; Yao *et al.*, 2006). It can be cheaply and broadly extracted from the empirical Green's functions calculated from cross-correlated ambient noise (Campillo and Paul, 2003; Shapiro and Campillo, 2004). Numerous studies have applied ambient noise surface-wave tomography to regional dense seismic array data to obtain detailed near-surface structures. (Lin and Ritzwoller, 2011; Chang *et al.*, 2016; Roux *et al.*, 2016; Liu *et al.*, 2017; Wang *et al.*, 2018; Mordret *et al.*, 2019; Fu *et al.*, 2022).

State-of-the-art ambient noise surface-wave tomography has provided valuable insights into complex near-surface systems (Roux *et al.*, 2016; Mordret *et al.*, 2019). However, methodological challenges persist in resolving shallow-depth shear-wave velocity (V_S) structures with high resolution (Share *et al.*, 2020). These include (1) insufficient resolution related to a narrow frequency range in dispersion spectrograms, particularly for complex velocity (Cheng *et al.*, 2023), and (2) the reliance on fundamental-mode surface waves alone cannot always provide sufficient constraints for inversion (Wiggins, 1972; Nolet and Panza, 1976; Maraschini *et al.*, 2010; Yokoi, 2010; Tomar *et al.*, 2018; Pan *et al.*, 2019).

Extracting high-quality phase velocity dispersion curves is essential to surface-wave methods. Numerous techniques have been developed for fundamental-mode extraction, including

1. Department of Earth and Space Sciences, Southern University of Science and Technology, Shenzhen, China, https://orcid.org/0009-0006-2319-5594 (SS); https://orcid.org/0000-0002-1243-8355 (ZL); https://orcid.org/0000-0003-4622-5988 (JC); https://orcid.org/0009-0000-0174-5870 (FJ); https://orcid.org/0000-0001-8681-8572 (CY); 2. Shenzhen Key Laboratory of Deep Offshore Oil and Gas Exploration Technology, Southern University of Science and Technology, Shenzhen, China; 3. Guangdong Provincial Key Laboratory of Geophysical High-Resolution Imaging Technology, Southern University of Science and Technology, Shenzhen, China

*Corresponding author: chenxf@sustech.edu.cn

the spatial autocorrelation method (Aki, 1957), the frequency–wavenumber (*f-k*) method (Capon, 1969; Lacoss *et al.*, 1969), the phase velocity image analysis (Yao *et al.*, 2006), and double beamforming (Roux *et al.*, 2016; Mordret *et al.*, 2019). To obtain dispersion curves with overtones, multichannel recording transformations such as the Radon transform method (RTM; Luo *et al.*, 2008) and the multichannel analysis of surface-wave (MASW) method (Park and Miller, 2008; Pan *et al.*, 2016) have been developed. With uniformly distributed stations, the *f-k* method can also extract overtones (Gabriels *et al.*, 1987; Mordret *et al.*, 2014). Wang *et al.* (2019) introduced the F-J method to extract Rayleigh dispersion curves with higher modes from ambient noise. This method is effective in resolving both Rayleigh- and Love-wave overtones (Hu *et al.*, 2020) from earthquakes (Zhou *et al.*, 2023) and ambient noise sources (Wang *et al.*, 2019; Li and Chen, 2020), and numerous studies updated this method from its original version (Dong *et al.*, 2021; Gao *et al.*, 2021; Song *et al.*, 2021, 2022; Xi *et al.*, 2021; Zhang *et al.*, 2022; Zhou and Chen, 2022). Applications of this method now include shallow subsurface exploration (Fu *et al.*, 2022; Li *et al.*, 2023) and continental lithosphere tomography (Wu *et al.*, 2020; Zhan *et al.*, 2020; Chen *et al.*, 2022; Wang *et al.*, 2024).

Several advantages drive our continued development of the F-J method for complex subsurface tomography. Although methods like *f-k*, MASW, and RTM can extract overtones, they depend on a 2D plane-wave assumption. In contrast, the F-J method, grounded in 3D wave propagation in a flat multilayered isotropic elastic model (Wang *et al.*, 2019), offers enhanced reliability for subsurface imaging. In addition, as noted by Share *et al.* (2020), travel-time-based imaging methods such as beamforming (Roux *et al.*, 2016; Mordret *et al.*, 2019) struggle to image low-velocity features because travel-time data are predominantly sensitive to higher velocity structures. This limitation underscores the value of non-travel-time-based methods such as the F-J method for complex structure tomography.

Similar to other surface-wave methods, dispersion extraction by the F-J method assumes a layered velocity structure. By applying the F-J transform to cross-correlation functions (CCFs) of an array, dispersion curves can be extracted to estimate the 1D velocity structure at the centroid of the array. This array-based nature requires dividing the array into subarrays for 3D modeling. Each subarray provides a local 1D velocity estimate and is then merged and interpolated to construct a 3D velocity model for the entire array. However, challenges in subarray selection persist. The subarray must be large enough to capture high-quality overtones and low-frequency dispersion curves but small enough to achieve adequate horizontal resolution and avoid the coverage of the subarray crossing two different 1D velocity structures.

The traditional array subdivision strategy of the F-J method tests various sizes and shapes, such as circular (Fu *et al.*, 2022) or square (Chen *et al.*, 2022), to identify suitable choices for specific research areas. Based on the test results, the array is subdivided into overlapping fixed-size and fixed-shape subarrays covering the entire area. Another method proposed by Li *et al.* (2023) estimates dispersion curves by stacking results of randomly generated subarrays. Although these methods can effectively find good subarrays for large-scale lithospheric tomography (Chen *et al.*, 2022; Ma *et al.*, 2022) and relatively uniform shallow structures (Fu *et al.*, 2022; Li *et al.*, 2023), they face challenges when imaging complex structures. The F-J method assumes a flat multilayered isotropic velocity structure, valid only when lateral velocity variations within the coverage of individual subarrays are sufficiently small. A synthetic test by Li and Chen (2020) demonstrated that when the F-J method is applied to subarrays covering two different layered structures, the resulting dispersion spectrogram combines dispersions from both structures, which is referred to as branched dispersion curves.

To find suitable subarrays adaptively instead of manual selection, which brings substantial workloads (Wang *et al.*, 2024; Yuan and Chen, 2024), we developed partition similarity test (PST). This method uses the dispersion similarity of different smaller subarrays to quantitatively measure structural homogeneity, judging their suitability to be combined into a larger subarray. Though the generated subarrays require rationale support by further research into the potential bias introduced by irregular shapes, this array subdivision approach offers a solution for applying the F-J method to complex environments.

Here, we apply the F-J method with subarrays generated by the PST the ambient noise data recorded at the Sagebrush flat site along the Clark fault branches of the San Jacinto fault zone (Ben-Zion *et al.*, 2015) to image the V_S structure. Numerous geophysical research have already been applied to study this array (Ben-Zion *et al.*, 2015; Hillers *et al.*, 2016; Roux *et al.*, 2016; Meng and Ben-Zion, 2018; Qin *et al.*, 2018; Mordret *et al.*, 2019; Share *et al.*, 2020; Touma *et al.*, 2021, 2022). Among these, the V_S structure (Mordret *et al.*, 2019) shows a divergence in a shallow low-velocity area compared to the V_P and resistivity inversion results (Share *et al.*, 2020). Our refined V_S model resolves this discrepancy and is consistent with the shallow structure review (Share *et al.*, 2020) at the low-velocity anomaly on both sides of the Clark fault and the trapping structure observed northeast of the Clark fault (Ben-Zion *et al.*, 2015; Qin *et al.*, 2018). This model images the underlying structure of a fault that is not field observed but inferred by topographic survey (Bevis *et al.*, 2005), and reveals clear lateral velocity variations along the Clark fault branches. Our case study demonstrates the ability of the new method in high-resolution imaging of shallow complex structures. The developed array subdivision method can be generally applied to adaptively identify suitable subarrays in dense arrays of various sizes and configurations.

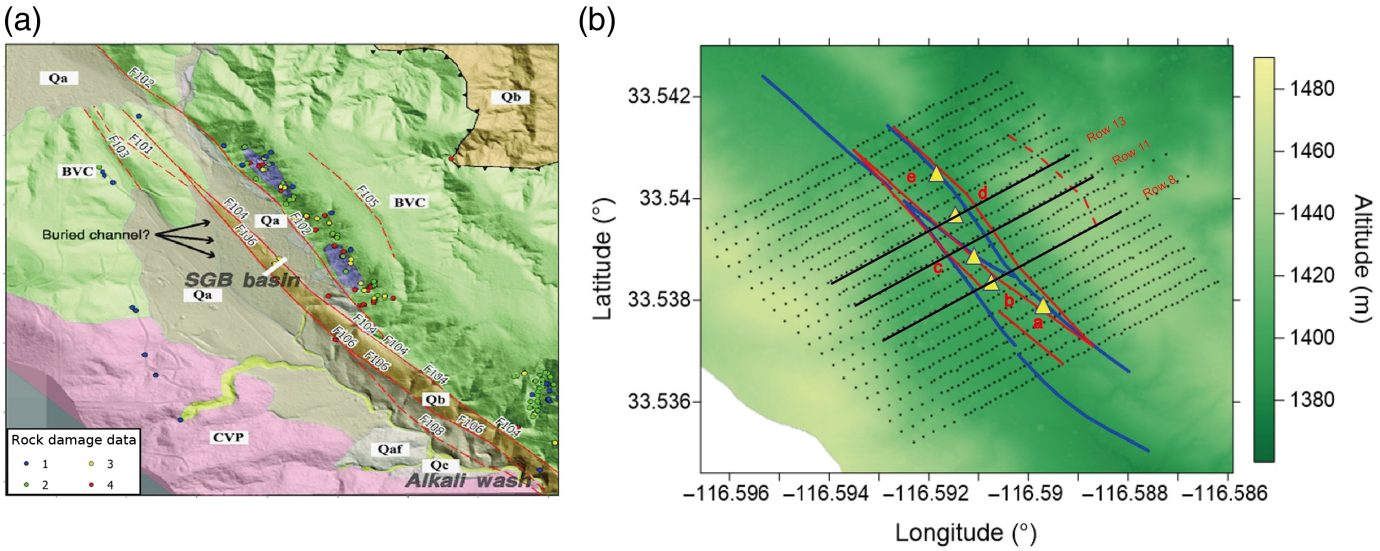

Figure 1. Geological and topographic data are analyzed here. (a) Lithology and damage intensity mapping at the surface modified from (Share *et al.*, 2020). The main geological/lithological units are Coahuila Valley Pluton (CVP, pink), Burnt Valley Complex (BVC, green), Quaternary sediments (Qa, gray), and Plio-Pleistocene Bautista Formation (Qb, brown). More differentiated sediments are alluvial fan (Qaf, gray) and colluvium (Qc, gray). The "buried channel?" indicates an inferred buried drainage channel containing more microfluids and conductive sediments than the rest of the Qa-SW unit. The colored dots indicate the damage intensity of the rock. The red solid line represents the strike-slip fault observed from the field by Wade (2018), and the red-dashed line represents the inferred faults not observed in the field. (b) Distribution of the dense seismic array used in this study. The background color is the relief calculated within a 10 m radius and topography from the B4 light detection and ranging (lidar) project (Bevis *et al.*, 2005). The blue solid lines are the surface traces for the Clark fault, referred to as F106, F104, and F102 from left to right by U.S. Geological Survey (USGS) (2006). The red solid lines are the same traces evaluated by Wade (2018) after a joint analysis of different research. The red dashed line represents the inferred fault trace. The black solid lines tagged by row numbers indicate the reference locations in Figure 10. The yellow filled triangles indicate the locations of the five stations we used for model validation in Figure S5. The color version of this figure is available only in the electronic edition.

Data and Methods

Sagebrush flat array

This study uses ambient noise data recorded by a dense nodal array with 1108 geophones in an ~600 m × 600 m configuration around the Clark fault branches of the San Jacinto fault zone at the Sagebrush flat (SGB) site for tomography. The array had an average 10 m row interstation and 30 m row separation and recorded vertical waveforms continuously at 500 Hz for about 1 month in 2014 (Ben-Zion *et al.*, 2015). After cutting the raw ambient noise data into hour-long segments, the CCFs between all station pairs were calculated by the open-source Python package CC-FJpy (Li *et al.*, 2021). Spectrum whitening was applied to reduce the effects of earthquakes and nonstationary noise sources (Bensen *et al.*, 2007). All hour-long CCF segments were stacked to improve the signal-to-noise ratio.

Bevis *et al.* (2005) conducted a high-resolution topographic survey of the San Andreas and San Jacinto fault zones in southern California to assess near-field ground deformation, with the relief details at the SGB site shown in Figure 1b. Wade (2018) analyzed the lithology and surface fault traces at the SGB site based on the V_S properties (Mordret *et al.*, 2019) and surface geological mapping results, as shown in Figure 1a (edit from Share *et al.*, 2020). Based on these analyses, three exposed branches of the Clark fault (F102, F104, F106) cross the array from northwest to southeast, whereas an inferred fault (F105) is situated to the northeast from the topographic survey (Bevis *et al.*, 2005).

F-J method

The CCF of ambient noise record is defined as

$$\tilde{C}(\boldsymbol{r},\omega) = U_1(\boldsymbol{x_1},\omega) * U_2(\boldsymbol{x_2},\omega), \quad (1)$$

in which $U_1(\boldsymbol{x_1},\omega)$ and $U_2(\boldsymbol{x_1},\omega)$ are the vertical component of seismic records at $\boldsymbol{x_1}$ and $\boldsymbol{x_2}$ in the frequency domain, ω is the angular frequency, and $\boldsymbol{r} = \boldsymbol{x_1} - \boldsymbol{x_2}$. Under the equipartition assumption (Campillo and Paul, 2003), the ambient seismic noise field is isotropic and stationary in space and time. Consequently, $\tilde{C}(r,\omega) = \tilde{C}(\boldsymbol{r},\omega)$, and $r = |\boldsymbol{r}|$ is the distance between two stations.

Similar to other ambient noise methods, the F-J method assumes a flat multilayered isotropic elastic model (Wang *et al.*, 2019). The CCFs are first retrieved from z-component ambient noise records, and a frequency–wavenumber transform is applied to CCFs to obtain the dispersion spectrogram $I(\omega,k)$, also known as the F-J spectrogram (Wang *et al.*, 2019):

$$I(\omega,\boldsymbol{k}) = \frac{1}{2\pi}\int_{-\infty}^{+\infty}\int_{-\infty}^{+\infty}\tilde{C}(r,\omega)e^{i\boldsymbol{k}\boldsymbol{r}}d\Sigma(\boldsymbol{r}). \quad (2)$$

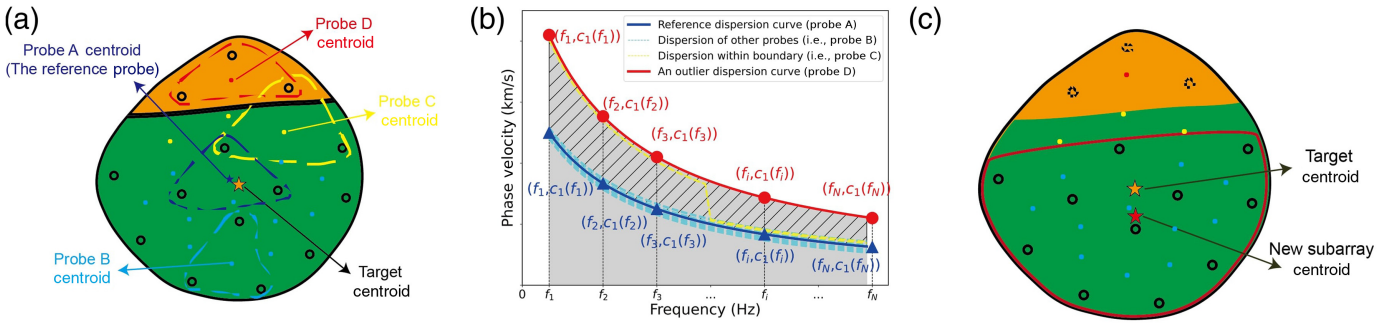

Figure 2. Illustration of the partition similarity test concept. (a) Target and probe definition: in the frequency–Bessel (F-J) method, the cross-correlation functions (CCFs) of a seismic station array are used to estimate the velocity structure at its centroid. Suppose there are some seismic stations (black hollow circles), and the covered area crosses two 1D velocity structures (orange and green background regions). The "target" refers to a relatively large seismic station array (in this case, all seismic stations are included). The target can be divided into smaller subarrays, called "probes" (e.g., three-station groups in this case), which enable localized dispersion curve extraction around the target centroid. Among these, the probe closest to the target centroid is designated as the reference probe (probe A). The relative error (RE) of all other probes is calculated with respect to probe A. Probes with the same velocity structure as probe A are marked in cyan, those crossing two structures are marked in yellow, and those covering a different structure are marked in red. (b) RE calculation: This panel illustrates the RE calculation and a hypothetical fundamental mode dispersion curve distribution of the probes in panel (a). The red dots and blue triangles represent dispersion points from an outlier and the reference probe, respectively. The slashed area denotes the absolute error (AE) between the curves. Dividing the AE by the entire gray area is defined as the RE, as approximated by equation (4). (c) New subarray formation: probes with similar dispersion curves (cyan centroids in panel a and corresponding cyan curves in panel b) are combined to form a new subarray. Note that this process excludes certain stations from the target, causing a centroid shift in the new subarray. The color version of this figure is available only in the electronic edition.

By transforming from Cartesian to cylindrical coordinates and assuming axial symmetry, the integral representation of zero-order Bessel function, $\frac{1}{2\pi}\int_0^{2\pi} e^{ikr\cos\theta}d\theta = J_0(kr)$, simplifies (2) to a 1D integral over the interstation distances (Wang *et al.*, 2019):

$$I(\omega,c) = \int_0^{+\infty} \tilde{C}(r,\omega)J_0\left(\frac{\omega}{c}r\right)rdr. \tag{3}$$

Here, $I(\omega,c)$ represents the F-J spectrogram for a given angular frequency ω and velocity c. Under the assumption that the CCF approximates the imaginary part of the Green's function in a flat multilayered elastic half-space, the Rayleigh-wave dispersion curves can be extracted as peak values of $I(\omega,c)$. Notably, this method retrieves not only the fundamental mode, but also overtone dispersion curves (Chen *et al.*, 2022) and even leaking modes (Li *et al.*, 2022). This study uses CC-FJpy (Li *et al.*, 2021) to implement the F-J method.

Criteria of similarity between two dispersion curves

To objectively evaluate the similarity between dispersion curves, a relative error (RE) is defined as follows:

$$\mathrm{RE} = \frac{\sum_{i=1}^{N}|c_1(f_i) - c_2(f_i)|}{\sum_{i=1}^{N}\max[c_1(f_i),c_2(f_i)]}, \tag{4}$$

in which f_1 to f_N represent the N picked frequency points for two dispersion curves, and $c_1(f_i)$ and $c_2(f_i)$ represent the corresponding phase velocity at f_i. Figure 2b illustrates the setup for equation (4), which quantitatively estimates the dissimilarity of dispersion curves on a scale from 0 to 1. Small RE indicates less discrepancy, whereas large RE indicates more discrepancy.

PST

The F-J method uses a subarray to estimate its centroid 1D velocity structure locally. The idea of the PST is to divide the subarray for more local estimation within the coverage of this subarray. A new subarray is generated by eliminating stations that produce dissimilar dispersion curves. The workflow consists of four steps:

First, the shape and size of "targets" and "probes" should be established, as shown in Figure 2a. A "target" refers to a relatively large subarray that is usually directly used for dispersion extraction in the traditional workflow of the F-J method (Chen *et al.*, 2022; Fu *et al.*, 2022). The shape of targets and probes can be tuned to the array distribution, such as a circle or square. Appropriate sizes of targets need to be tested to produce a better dispersion spectrogram (Chen *et al.*, 2022; Fu *et al.*, 2022). A helpful starting point is applying the F-J method to the entire array, with the first branched fundamental-mode dispersion point revealed by the dispersion spectrogram indicating the lower limit of the resolvable frequency range. Targets are fixed-shape subarrays with sufficient aperture to capture the phase velocity at the minimum frequency ($f_{\min}$). The suitable aperture ($r_{\max}$) of the array can be estimated by the minimum

target frequency $f_{\min}$, which is considered at least half of the wavelength ($\lambda_{\max}$) at the $f_{\min}$ in this study:

$$r_{\max} \geq \frac{\lambda_{\max}}{2} = \frac{c(f_{\min})}{2f_{\min}}, \tag{5}$$

in which c is the phase velocity of the surface-wave fundamental mode. "Probes" are smaller subarrays with centroids located within a target. These provide more local dispersion estimations within the target coverage. The probe size is determined by the branched frequency range, that is, f_1 to $f_N$of the target dispersion spectrogram (Fig. 2b), ensuring accurate dispersion extraction using the same criteria as in equation (5). In addition, the aperture of the probe will be the smallest resolvable structural unit of the obtained velocity model.

Second, the RE of each probe is calculated within the target by comparing its dispersion curve against that of the reference probe, the one nearest to the centroid of the target (probe A in Fig. 2a). As shown in Figure 2a,b, probes with similar velocity models will produce comparable dispersion curves (e.g., probe B in Fig. 2a), whereas dissimilar ones (e.g., probes C and D in Fig. 2a) will exhibit larger RE values.

Third, an error threshold is established, and probes with small RE values are combined into a new, larger subarray. For this study, probes in cyan in Fig. 2c represent those with RE values below the empirically determined threshold of 0.05, forming the refined subarray. The robustness of this threshold is discussed in section 4.3.

Fourth, quality control is applied to remove or adjust unsatisfactory subarrays. In transition zones, some probes may still show branched dispersion curves in their dispersion spectrograms (e.g., when probe C in Fig. 2a serves as the reference probe as probe A), resulting in the acceptance of only a few or disconnected probes. Therefore, only subarrays formed by more than four adjacent probes are retained for analysis. In addition, the dispersion spectrograms of these new subarrays are examined manually to confirm that there is no branched dispersion. For those generated subarrays that remain having branched dispersion curves on their dispersion spectrograms, error thresholds between 0.03 and 0.08 will be applied and tested again.

Multimodal dispersion picks and inversion

This study employs a quasi-Newton method to invert 1D V_S model based on the Broyden–Fletcher–Goldfarb–Shanno (BFGS) correction (Byrd *et al.*, 1995). Pan *et al.* (2019) presented the misfit function for multimodal surface-wave dispersion as follows:

$$f(V_S) = \frac{1}{m}\sum_j A_j \left\{ \sum_i (c_{ij}^s(V_S) - c_{ij}^0)^2 \right\} + \alpha ||\nabla \cdot V_S||, \tag{6}$$

in which V_S represents the shear-wave velocity model, i is the frequency sampling point, j is the mode of the dispersion curve, c_{ij}^s is the synthetic phase velocity, c_{ij}^0 is the observed phase velocity, and A_j is the weight of the jth mode. $||\nabla \cdot V_S||$ is the derivate damping term, which is the L2 norm of the spatial Laplacian of V_S, and α is set to be 0.1 based on the L-curve criteria (Pan *et al.*, 2019). We adopt a layered model with a 5 m thickness for each layer, inverting to a depth of 300 m. To ensure robust convergence and avoid local minima, we perform multimodal dispersion curve inversion using 80 randomized starting models, with velocity varying of each layer by up to 0.8 km/s from a reference model, following Mordret *et al.* (2019).

A careful overtones selection is essential because an inversion of spurious estimates often results in more significant misfits and worse dispersion fitness (Li *et al.*, 2022). Limited by the complex velocity structures and strong crossed artifacts caused by insufficient space sampling for dispersion curves of high frequency (Cheng *et al.*, 2023), continuous overtones cannot be directly determined for each subarray, and some modes are missing or mixed. Given the stability and broader frequency range coverage of the fundamental mode, overtones are auxiliary information to refine details. Therefore, we assign weights of four to the fundamental mode and one to each overtones in equation (6), while implementing a conservative dispersion-curve picking and examination strategy: first, only the fundamental dispersion is picked and inverted for a reference velocity referred to as V_S^{fund}. Next, theoretical overtones are calculated from V_S^{fund}, identifying relevant overtone strips in the dispersion spectrogram. A joint inversion of fundamental mode and overtones is performed to obtain a new velocity structure referred to as V_S^{over}. Finally, the misfit of V_S^{over} compared to V_S^{fund} and the fit of the fundamental mode are assessed to examine the quality of the overtone data.

Workflow of FJ-PST

The process of integrating the FJ method with PST (FJ-PST) to obtain a 3D V_S model involves four main steps, as illustrated in Figure 3 for the application in the SGB array. First, subarrays are adaptively generated using the PST method. To determine an appropriate target size, the entire array is initially analyzed using the F-J method. The dispersion spectrogram of the entire array (Fig. S1b1, available in the supplemental material to this article) showed that the first branch is around 3 Hz, indicating the minimum resolvable frequency band. Based on the maximum phase velocity of ~900 m/s observed in Figure S1b1, the minimum aperture of the subarray estimated by equation (5) is about 150 m. Given the approximately square shape of the array and its uniform station spacing, square-shaped targets with a side length of 120 m (an aperture of 170 m) were selected (yellow dots in Fig. 3a).

Probes are set to squares of 60 m because branching typically occurs between around 9 and 16 Hz (Fig. S1b2), requiring a subarray aperture of around 50 m by equation (5), based on the highest phase velocity of ~800 m/s observed among all targets at 9–10 Hz. Setting probes to squares of 60 m (brown dots in Fig. 3a) ensures accurate extraction of dispersion curves for

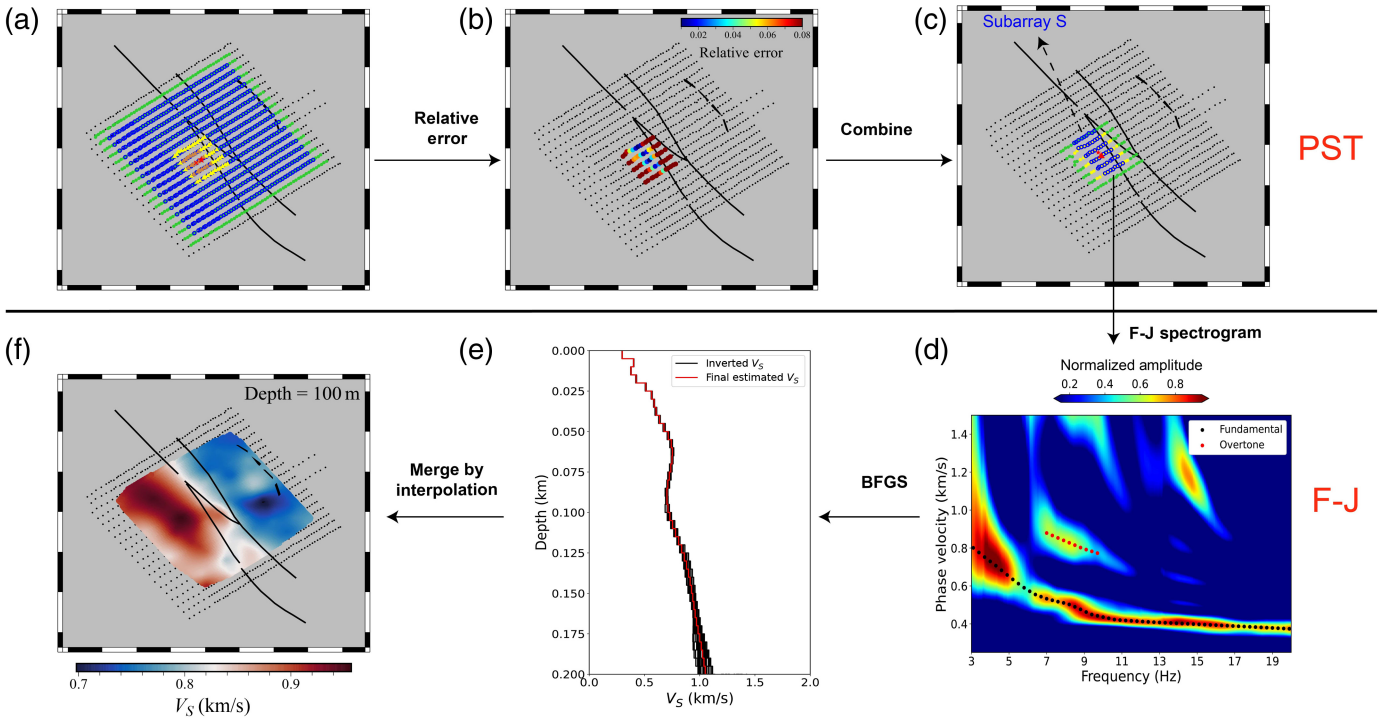

Figure 3. Illustration of the 3D V_S model retrieval from ambient noise data using FJ-PST in this study. (a) The set of targets and probes. The black dots represent array stations, solid lines indicate fault branches, and dashed lines mark inferred faults, as shown in Figure 1a. The green dots and hollow blue circles indicate the centroids of all targets and probes, respectively, used in this study. The yellow triangles represent stations of a sample target, and brown triangles represent stations of a sample probe used to test this target. The centroid of the sample target and probe is marked with a red star and a red cross, respectively. (b) The distribution of RE for probes within this target. (c) A generated subarray "S" for the sample target. The yellow dots show stations of the sample target, green dots represent stations from all probes for the target, and blue dots mark stations in the generated subarray. (d) The dispersion spectrogram calculated from CCFs of subarray S. (e) 1D V_S model from the inversion of multimodal dispersion curves with the Broyden–Fletcher–Goldfarb–Shanno method. (f) A depth slice at 100 m of the final 3D V_S model by merging 1D V_S models at all reference locations by Kriging interpolation. The color version of this figure is available only in the electronic edition.

this frequency range. Subsequently, all possible targets and probes are generated to maximize data utilization and enhance lateral resolution, as shown in Figure 3a–c.

Second, the F-J transform is applied to the CCFs of each subarray to obtain dispersion spectrograms (Fig. 3d). Third, multimodal dispersion curves are picked and examined, and the BFGS method is used to invert these curves to derive the 1D V_S structure for each subarray (Fig. 3e). Finally, all 1D V_S structures are merged using Kriging interpolation to construct the final 3D V_S model (Fig. 3f).

Results

Phase velocity

Figure 4a–c shows the Rayleigh-wave fundamental-mode phase velocity at 4, 8, and 15. At 8 and 15 Hz, two significant low-velocity anomalies are present on either side of the Clark fault. The anomaly on the northeast side persists at 4 Hz, whereas the southwestern anomaly diminishes at this frequency. The southwestern and northwestern corners remain at high velocities within all presented frequency ranges. The observed highest mode for each subarray is plotted in Figure 4d. The overall fundamental-mode phase velocity distribution aligns well with the geological units.

3D shear-wave velocity structure

Representative vertical slices of the final 3D V_S model are shown in Figure 5, offering perspectives from southwest and southeast. Representative depth slices of the final 3D V_S model are presented in Figure 6.

From 10 to 40 m depth, the Clark fault is characterized by high velocity. At the same time, the V_S structure contains two low-velocity anomalies on both sides of the fault branches (Figs. 5a and 6a). The patterns of these two low-velocity anomalies gradually diminish from 50 to 100 m (Fig. 6b). In contrast, two other low-velocity anomalies emerge on the northeast side of the Clark fault, one at the southeast corner ranging from 50 to 100 m, whereas another underneath the northeast of the Clark fault ranges from 70 to 100 m (Fig. 6b,c). Lower than 80 m, two low-velocity anomalies are located at the center of the Clark fault and beneath the inferred fault, respectively (Figs. 5b and 6c).

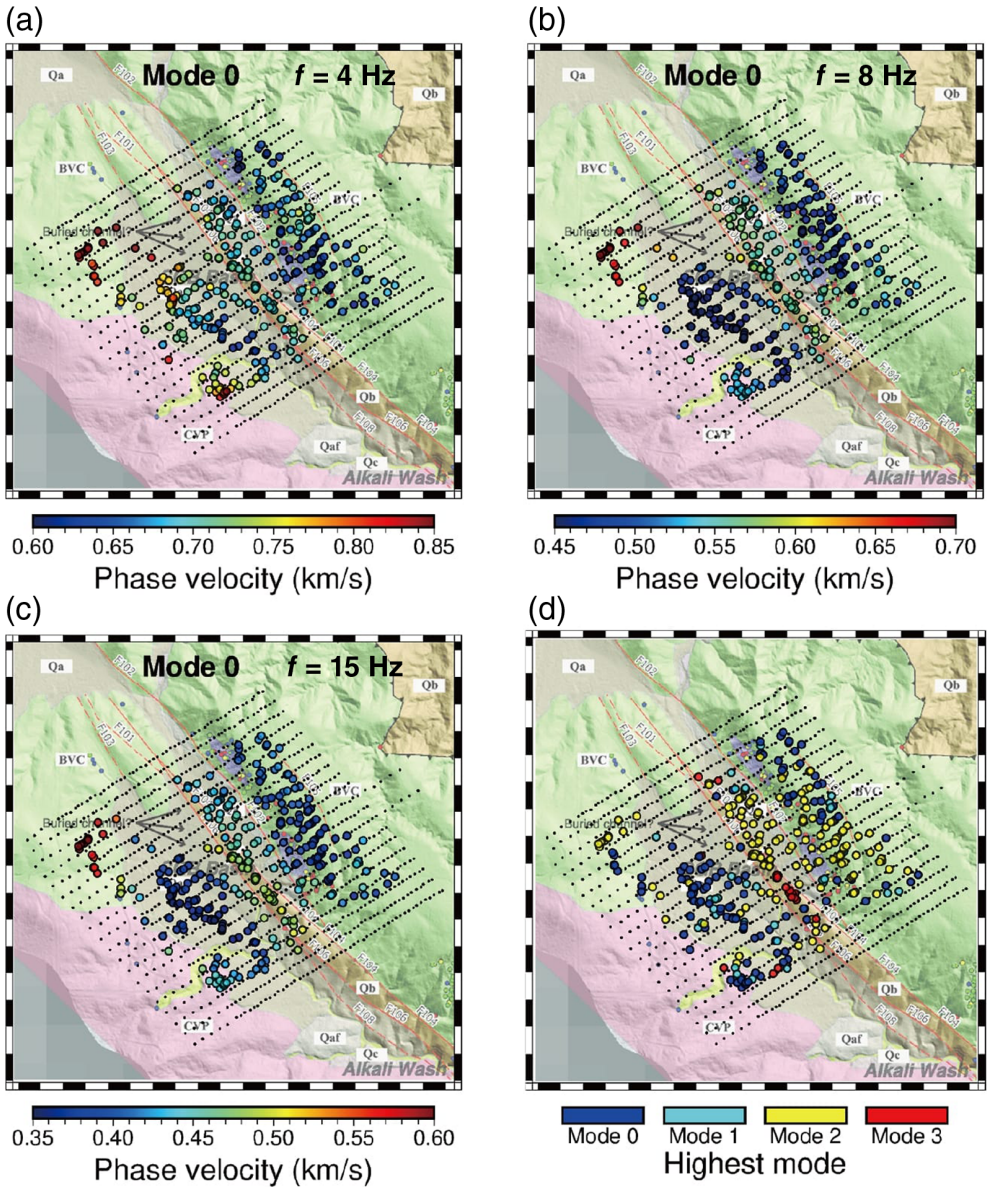

Figure 4. The phase velocity maps for the Rayleigh-wave fundamental mode at (a) 4 Hz, (b) 8 Hz, and (c) 15 Hz. The highest mode extracted for each subarray is shown in (d). The background image for each figure is edited from Share *et al.* (2020). The color version of this figure is available only in the electronic edition.

Discussion

Effectiveness of overtones

Overtones of dispersion curves offer additional constraints for inversion alongside the fundamental mode. In this study, due to the complex geological structures and prominent crossed artifacts, many overtones can only be identified in limited segments, as the example presented in Figure 3d. Figure 7 compares inversion results obtained using the fundamental mode alone with those incorporating multiple modes for the representative subarray "S" (shown in blue dots of Fig. 3c) and a sensitivity analysis. Even when integrating only a short segment of overtones, the resulting velocity structure captures more detailed features in the shallow structure (from 30 to 100 m), and the standard deviation is significantly reduced, demonstrating the value of overtone inclusion.

Comparison between FJ-PST and the traditional F-J method

The synthetic test by Li and Chen (2020) has demonstrated the importance of subarray selection when applying the F-J method to complex structures, highlighting the issue caused by subarrays crossing two different layered velocity structures. Here, we illustrate the effectiveness of FJ-PST by comparing it to the dispersion spectrogram of the traditional F-J method in this array. As shown in Figure 8, the traditional F-J method with fixed-shaped subarrays results in branched fundamental-mode dispersion curves, whereas FJ-PST effectively identifies boundaries and adaptively adjusts subarrays to mitigate this issue. More cases across different areas of the array and the corresponding improvement of FJ-PST can be found in Figure S2.

Error threshold

One primary step in the PST is combining the accepted probes into a new subarray. Although the 0.05 threshold used in this study is empirical, it is important to emphasize the robustness of the F-J method: the removal or addition of certain seismic stations has a negligible impact on dispersion extraction as long as the structure can be treated as a 1D layered velocity model. Therefore, the goal of PST is not to identify the "best" subarray for a given target, but to select suitable probes by excluding stations that would create an array over different 1D velocity structures. Because probes across different structures typically show significant dispersion dissimilarity, a wide range of error thresholds can effectively detect and eliminate unwanted probes.

Figures S3 and S4 present error threshold tests for two subarrays: one exhibiting branched dispersion curves and

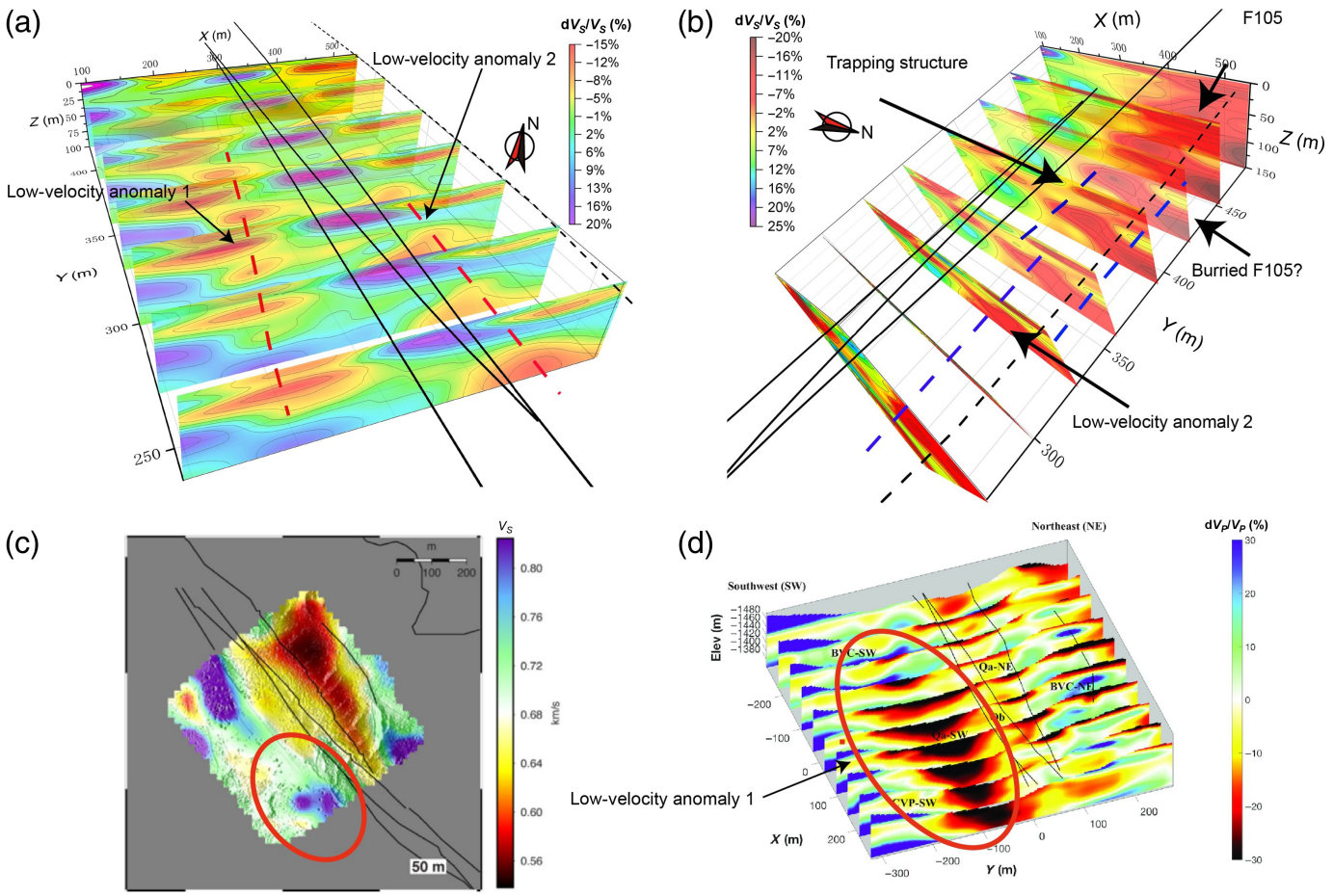

Figure 5. Representative vertical slices of the final 3D V_S perturbation model from the inversion of multimodal dispersion curves, shown from two perspectives: (a) southwest and (b) southeast. The black solid lines indicate fault traces evaluated by USGS (2006), and the black dashed line marks the inferred fault trace F105 Wade (2018). The red dashed lines in (a) denote two low-velocity anomalies identified in the model, and blue dashed lines in (b) mark features including a trapping structure, low-velocity anomaly 2, and a buried F105. The "?" in (b) points to "Burried F105," which indicates the possible location of an inferred fault (F105) identified by sharp lineaments in the topographic survey (Bevis *et al.*, 2005). (c) The V_S velocity map obtained from Mordret *et al.* (2019) at 50 m depth (edited from Share *et al.*, 2020). (d) The V_P velocity perturbation model obtained by Share *et al.* (2020). The red ellipses mark the velocity discrepancy between (c) and (d). The color version of this figure is available only in the electronic edition.

one without. In both cases, although some differences in subarrays occur when thresholds are set between 0.03 and 0.08, these variations have minimal impact on the dispersion extraction of the dispersion spectrogram. Most importantly, in all scenarios, the subarrays effectively avoid stations that could negatively affect the new dispersion spectrogram (i.e., cause branched dispersion curves).

Subarray distributions

Current state-of-the-art surface-wave theories are based on the flat multilayered isotropic structure assumption, which complicates the extraction of dispersion curves in geologically interesting transition zones where the velocity structure changes laterally. Although it is possible to extract low-quality dispersion curves in these areas, they may yield biased interpretations of the underlying structures. Further research is needed to develop methods to capture velocity structures in these transitional regions accurately.

In this study, the PST method offers an alternative solution by enabling array-based methods to avoid direct measuring phase velocities within transition zones and instead estimate these areas through interpolation. However, the interpolated structures lack the same reliability as directly measured data, and, here, we introduce a model credibility assessment.

Because the dispersion curve extracted from each subarray provides a local 1D estimate of the velocity structure at its centroid location, a higher density of centroids within a given area yields richer observational data. In contrast, regions containing fewer subarrays or lacking observations likely correspond to structural boundaries and are estimated via interpolation. Consequently, areas with denser observations yield more reliable velocity estimates. We quantify this observation density as follows: first, the model coverage is defined as the area of the

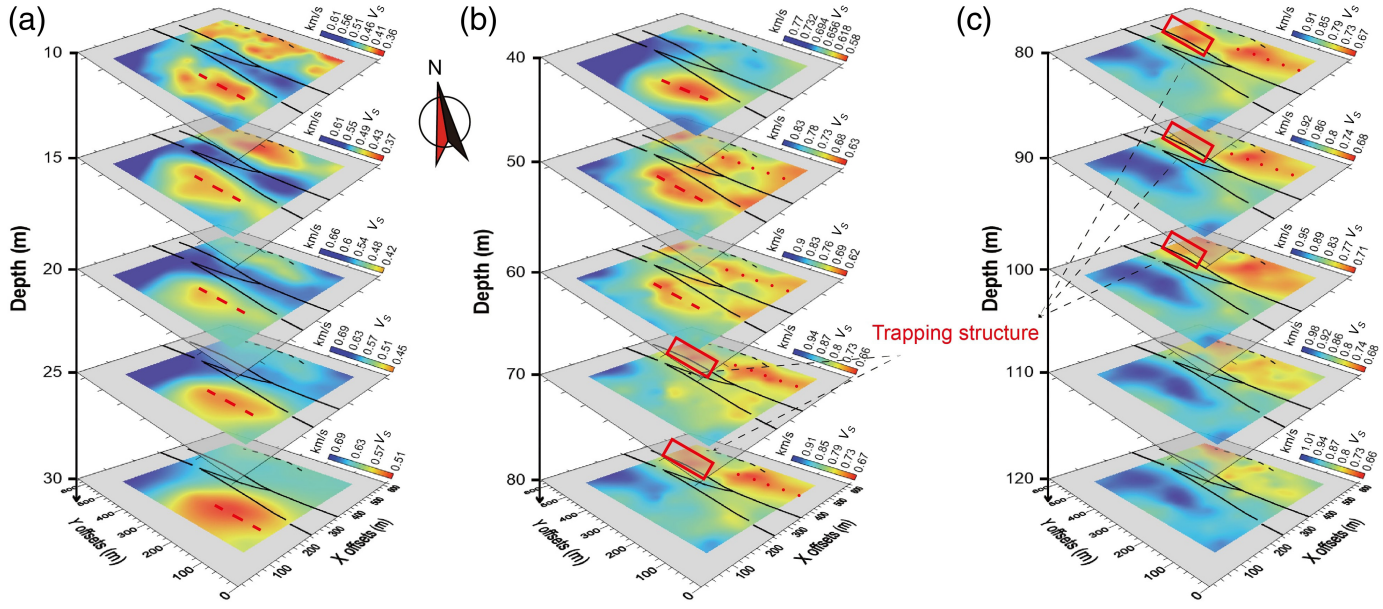

Figure 6. Depth slices of the final 3D V_S model from multimodal dispersion curve inversion at three depth ranges: (a) 10–30 m, (b) 40–80 m, and (c) 80–120 m. The red dashed line represents the low-velocity anomaly 1; the red dotted line indicates low-velocity anomaly 2; and the red rectangles indicate the low-velocity trapping structure inferred by fault zone trapped waves (Qin *et al.*, 2018). The color version of this figure is available only in the electronic edition.

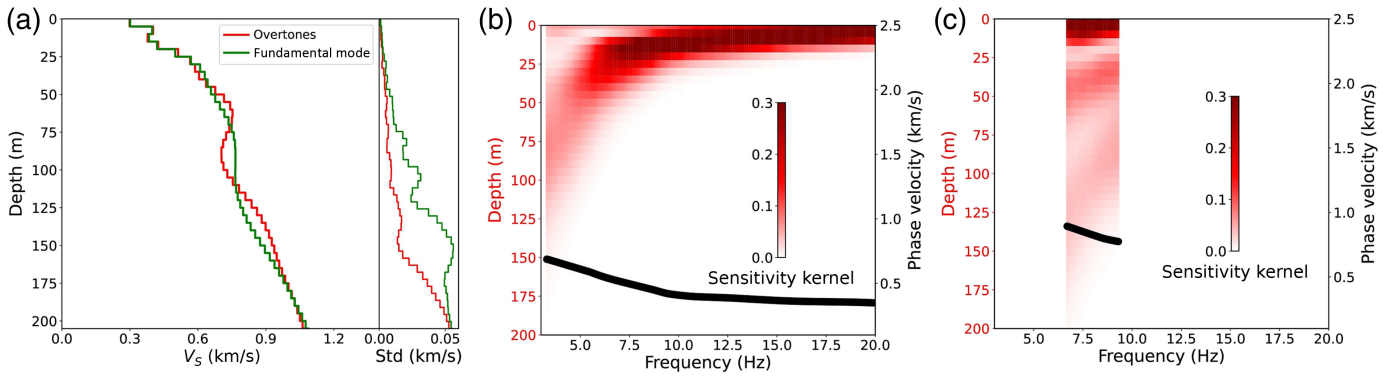

Figure 7. The effectiveness of overtone and dispersion sensitivity analysis. (a) Comparison of the 1D V_S model inverted with and without overtones extracted in Figure 3d. (b) The sensitivity kernel of the dispersion curve for the fundamental mode, and (c) the overtone. The red-shaded areas illustrate the sensitivity distributions as a function of depth and frequency, and the black points indicate the selected dispersion curves for each mode, as shown in Figure 3d. The values for each dispersion curve are shown on the right-side vertical axes. The color version of this figure is available only in the electronic edition.

V_S model derived from inversion and interpolation. To simplify calculations, we compute the density only at the locations of stations within this coverage (see black dots within the colored area in Fig. 9a). For the location of each station, we count the number of subarrays for which centroids fall within a unit aperture of 60 m (the side length of the probe), which serves as the resolution unit for this model. Next, we determine the maximum number of such subarrays across the entire region. Finally, we normalize the counts across the region by this maximum value and define them as the subarray density.

The density plot is illustrated in Figure 9a. As anticipated, the density within each unit is higher, whereas the unit boundaries (transitional zones) exhibit low density. The V_S model in regions identified with low subarray density (e.g., structural boundaries or near-fault blind spots; see Fig. 9b and Fig. S6) relies more heavily on interpolation and carries higher uncertainty. This is exemplified by the bimodal low-density area on the southeast, which corresponds to the boundaries between the Burnt Valley Complex (BVC), Coahuila Valley Pluton (CVP), and southwestern Quaternary sediments (Qa-SW)

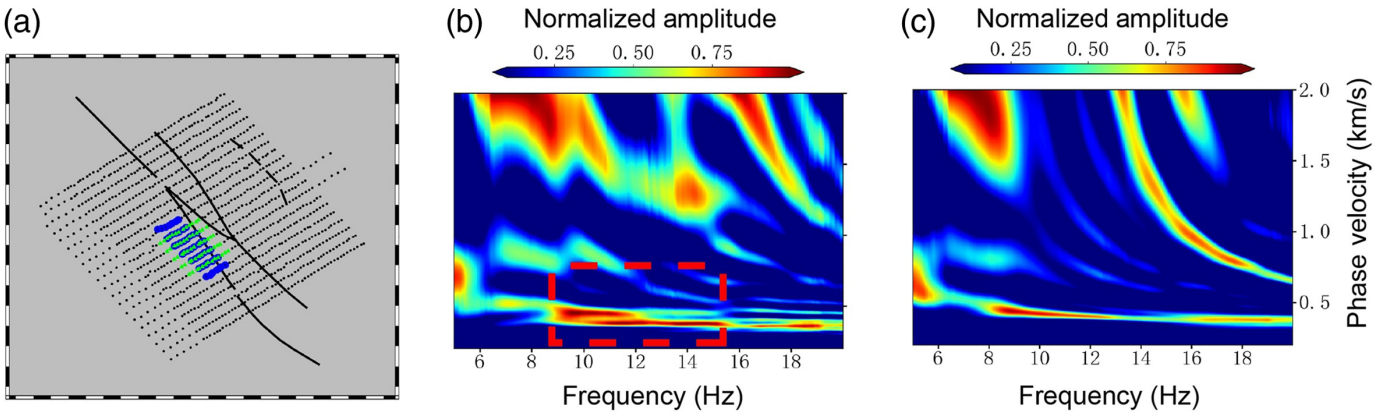

Figure 8. Comparison between FJ-PST and the traditional F-J for the dispersion spectrogram improvement. (a) Subarrays of FJ-PST (blue) and the nearest subarrays of traditional F-J (green). (b) Dispersion spectrogram calculated by the F-J for the green subarrays in panel (a), with red-dashed squares indicating the branched fundamental mode. (c) Dispersion spectrogram calculated by the F-J for the blue subarrays in panel (a). The color version of this figure is available only in the electronic edition.

units. Similarly, the curved low-density region on the right edge aligns with the abrupt velocity change across F105. These observations demonstrate that the PST is sensitive to boundaries between geological units without requiring prior information.

A further comparison between the phase velocity distribution of the Rayleigh-wave fundamental mode at 15 Hz and the observed geological units is presented in Figure 9b. Significant phase velocity contrasts are observed across different units. For instance, the BVC units in the northwestern corner exhibit very high phase velocities, whereas the Qa-SW and BVC units in the northeastern region show very low phase velocities. However, within each individual unit, the velocity variations are relatively minor. This explains why the PST can effectively detect boundaries because phase velocities typically undergo dramatic changes when transitioning between different geological units.

A significant low-density region is identified at the top edges of Figure 9a, which we designate as the northwestern complex zone (CPZ-NW). Geological observations in Figure 9b indicate that the CPZ-NW is linked to two inferred fault traces, F101 and F103, and a mixture of BVC and Qa rock units. The complex geological morphologies will likely result in significant velocity variations, making them unsuitable for applying the F-J method with the current probe and target sizes. Consequently, the PST accepted only a few subarrays in this region. Figure 9e,f provides examples of two subarrays located in the CPZ-NW (subarrays B and C in Fig. 9c). The corresponding dispersion spectrograms indicate low-quality dispersion curves and significant branched fundamental modes in multiple frequency bands, beginning at around 9 Hz. Figure S6 provides five probes within the CPZ-NW; the corresponding dispersion spectrogram still has branched dispersion curves within the tested band. These are the cases when probe C in Figure 2a serves as the reference probe and thus does not find nearby probes with small RE.

The continuous high density observed along the Clark fault branches in Figure 9a raises an interesting point because the PST is expected to result in a low-density area along the middle three fault branches as other geological boundaries. This indicates neither a failure of the PST nor the absence of F104 because the analysis was limited to the 3–16 Hz frequency band. Extensively branched dispersion is primarily observed between 9 and 16 Hz for the regular-shape subarrays (targets, i.e., Fig. 8b), motivating us to perform PST within this frequency range. Zooming-in on the phase measurements at 15 Hz in Figure 9b, the differences between the two sides of F104 exist but are relatively small compared to those observed across other boundaries.

As indicated by a subarray located at the trifurcated branches (the subarray A in Fig. 9c), the obtained dispersion spectrogram (Fig. 9d) does not have severe branched dispersion curves between 9 and 16 Hz but begins from 17 Hz. This higher branched band is sensitive to a shallower variation that is beyond the vertical resolution here. A different test band and probe size should be used for PST if a dispersion higher than 16 Hz is wanted, and show that the shallow part in this area (<60 m) does not exhibit significant changes compared to other geological boundaries, and prominent variations become apparent deeper than 80 m. This relatively uniform shallow velocity provides F-J with more accepted subarrays at the Clark fault, revealing a deeper variation with higher resolution.

Important shallow geology structures

Based on the 3D V_S model, several primary geological structures are observed:

1. Low-velocity anomaly 1: As illustrated in Figures 5a and 6a,b, a buried low-velocity channel is situated in the southwest (referred to as low-velocity anomaly 1), ranging in depths from 10 to 60 m. Previous research highlighted this

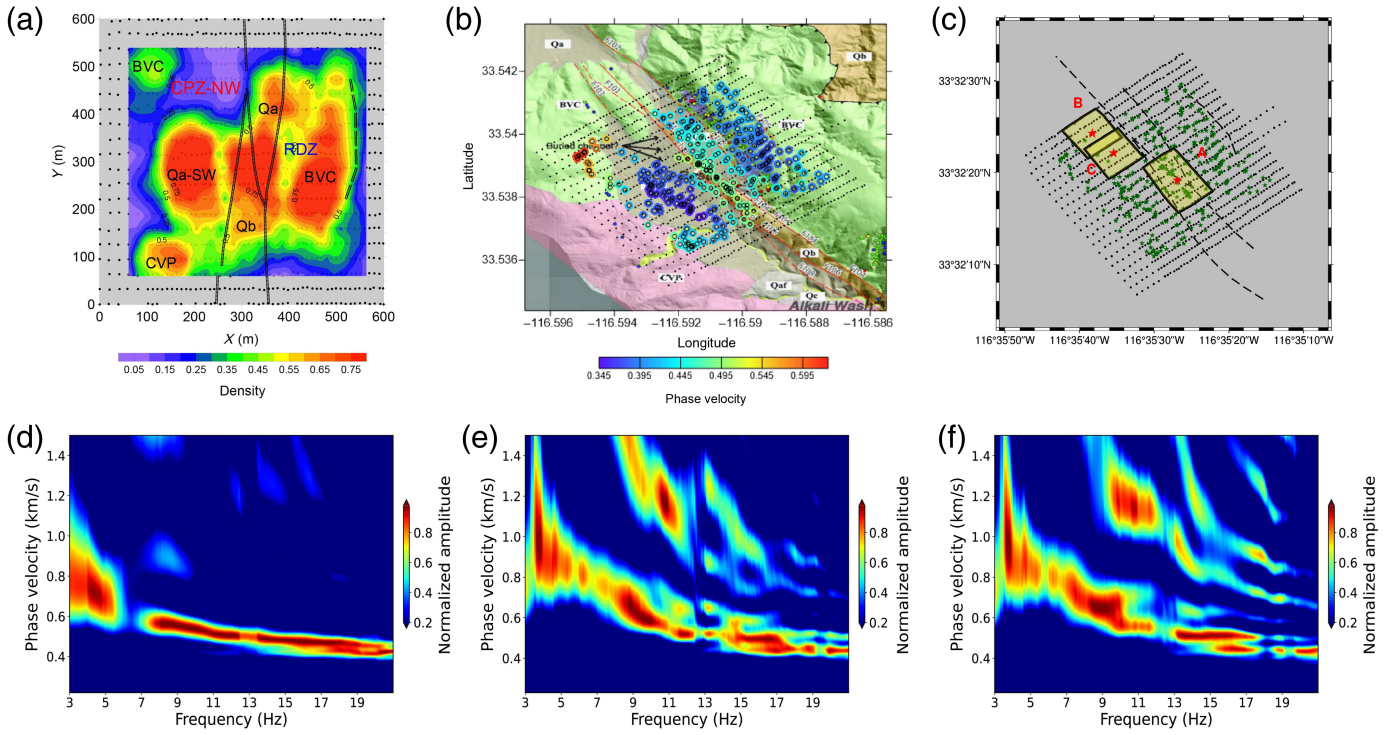

pattern by a *P*-wave low-velocity anomaly (Fig. 5d) and a low-resistivity feature (Share *et al.*, 2020). However, the previous V_S model obtained by Mordret *et al.* (2019) in the depth slice at 50 m (Share *et al.*, 2020) does not depict this structure (Fig. 5c), and our tomography results resolve this discrepancy.

2. Low-velocity anomaly 2: As depicted in Figures 5b and 6b,c, another deeper low-velocity anomaly (referred to as low-velocity anomaly 2) is situated on the right side of the middle fault traces, ranging from 50 to 90 m. The V_S model of Mordret *et al.* (2019) exhibits a general pattern consistent with this observation (Fig. 5c).
3. The trapping structure: Ben-Zion *et al.* (2015) and Qin *et al.* (2018) noted a low-velocity trapping structure to the northeast of the fault traces. Our results exhibit this pattern at depths from 70 to 100 m, as shown in Figures 5b and 6b,c. We find it interconnects with low-velocity anomaly 2 but displays a lower velocity anomaly and offsets horizontally and vertically.
4. The inferred fault F105: Identified by sharp lineaments from the topographic survey (Bevis *et al.*, 2005), an inferred fault trace (F105 in Fig. 1a) is situated in the northeastern corner of the array. Our V_S tomography confirms its presence, revealed by the northeastern low-velocity anomaly from 10 to 25 m in Figure 6a. Interestingly, this structure becomes less distinct below 30 m but gradually becomes more pronounced after 100 m (Fig. 6c). We attribute this depth-dependent resolution to the combined effects of low-velocity anomaly 2 and the trapping structure, which obscure the fault expression at intermediate depths.

Figure 9. The relationship between geological units and partition density. (a) The partition density plot for the model coverage. The main geological units are marked in black, and the RDZ is marked in blue. A significant low-density area is highlighted in red: CPZ-NW. (b) The phase velocity distribution of Rayleigh-wave fundamental mode at 15 Hz is plotted at the original geology unit plot by Share *et al.* (2020). (c) Example subarrays: subarray A is located within the Clark fault, and subarrays B and C are located in the CPZ-NW. The subarrays consist of stations (black dots) covered by yellow areas, with the red star indicating the centroid of each subarray. (d–f) The dispersion spectrograms obtained by the F-J method for subarrays A, B, and C, respectively. The color version of this figure is available only in the electronic edition.

Structures within the branches of Clark fault at the SGB site

To better visualize the lateral variation of the Clark fault at the SGB site, we plot three vertical V_S slices where three fault branches (F106, F104, and F102) intersect (Fig. 10), with black reference lines in Figure 1b indicating their locations. Evaluations of two surface fault traces are marked in gray and black dashed lines (Dor *et al.*, 2006; U.S. Geological Survey [USGS], 2006). Our results show significant along-strike variations along branch F104 below 60 m depth. The southern segment (rows 8-11) exhibits particularly strong velocity contrasts, which become weaker in the direction northward (row 13).

We use the waveform simulation method proposed by Lu and Ben-Zion (2022) to validate this high-resolution variation. We choose five stations distributed along and within the fault

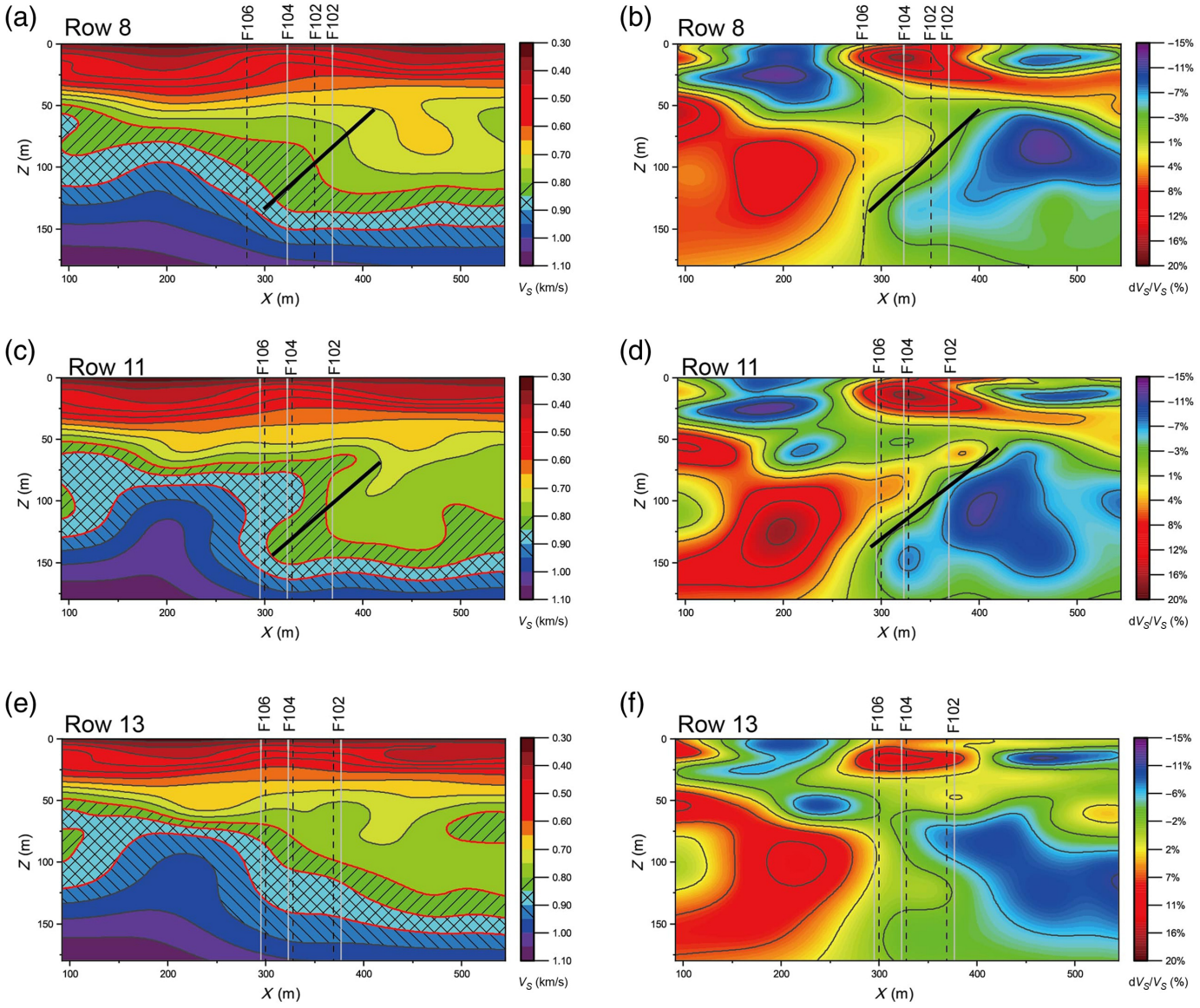

Figure 10. Vertical slices of (a,c,e) V_S model and (b,d,f) V_S perturbation within the mixture branches of F106, F104, and F102 (referenced in Fig. 1b as rows 8, 11, and 13). The black dashed vertical lines and gray solid lines in each plot represent the fault traces estimated by USGS (2006) and Wade (2018), respectively. Three velocity contours are typically marked in panels (a) as different filling lines to visualize the variations better. The black solid lines indicate the high-resolution variation along the fault branches under F104. The color version of this figure is available only in the electronic edition.

branches (reference locations in Fig. 1b) to synthesize the CCFs using the finite-difference method (Zhang and Chen, 2006; Zhang *et al.*, 2012). The synthesized CCFs are compared with the observed in three different frequency bands (3–7 Hz, 7–12 Hz, and 10–15 Hz). As illustrated in Figure S5, while slight time delays and waveform mismatches exist, the synthetic CCFs align well with the observed data, supporting the accuracy of our inferred model.

Conclusions

In this study, we propose a quantitative PST to adaptively address the branch dispersion phenomenon of the dispersion spectrogram when applying the F-J method to complex structures. To validate its effectiveness, the method is utilized to image the V_S structure at the SGB site, located along the Clark fault branches of the San Jacinto fault zone. The PST generates subarrays that extract continuous Rayleigh-wave fundamental modes from 3 to 16 Hz and fragmental overtones. The inversion result resolves a discrepancy between the V_S model and other geophysical observations, presenting higher resolution geological characteristics and revealing detailed structures of the Clark fault at shallow depths. The density information of subarray centroids is employed to evaluate the model credibility and guide further improvements, such as exploring different targets and probes or conducting joint analyses with

other methods. Based on this case study, we consider this method a valuable tool for overtone surface-wave tomography in imaging complex subsurface structures. The developed array subdivision method can be applied to adaptively identify suitable subarrays in dense arrays of various sizes and configurations beyond the scope of this case study.

Data and Resources

The seismic data used in this article can be obtained from the Data Management Center (DMC) of the Incorporated Research Institutions for Seismology (IRIS) and Broadband Seismic Data Collection Center (Vernon *et al.*, 2014) via doi: 10.7914/SN/ZG_2014, and the IRIS DMC via https://ds.iris.edu/mda/9A/156/. The CC-FJpy (Li *et al.*, 2021) which was used for cross correlation and F-J calculation can be obtained from https://github.com/ColinLii/CC-FJpy. Both websites were last accessed in December 2023. The supplemental material includes a detailed comparison of dispersion spectrograms for different subarray sizes, improved examples of spectrograms using the FJ-PST method, and error threshold tests. Additionally, it presents the results of waveform fitting for different virtual sources and provides dispersion spectrograms of probes located within the CPZ-NW.

Declaration of Competing Interests

The authors acknowledge that there are no conflicts of interest recorded.

Acknowledgments

The authors thank two anonymous reviewers for their constructive comments and suggestions. This work was supported by the National Key Research and Development Program of China (2022YFC3003504), the Guangdong Provincial Key Laboratory of Geophysical High-resolution Imaging Technology (2022B1212010002), and the Shenzhen Key Laboratory of Deep Offshore Oil and Gas Exploration Technology (ZDSYS20190902093007855). The numerical calculations were supported by Center for Computational Science and Engineering at Southern University of Science and Technology.

References

Aki, K. (1957). Space and time spectra of stationary stochastic waves, with special reference to microtremors, *Bull. Earthq. Res. Inst.* **35,** 415–456.

Bensen, G. D., M. H. Ritzwoller, M. P. Barmin, A. L. Levshin, F. Lin, M. P. Moschetti, N. M. Shapiro, and Y. Yang (2007). Processing seismic ambient noise data to obtain reliable broad-band surface wave dispersion measurements, *Geophys. J. Int.* **169,** no. 3, 1239–1260, doi: 10.1111/j.1365-246X.2007.03374.x.

Ben-Zion, Y., F. L. Vernon, Y. Ozakin, D. Zigone, Z. E. Ross, H. Meng, M. White, J. Reyes, D. Hollis, and M. Barklage (2015). Basic data features and results from a spatially dense seismic array on the San Jacinto fault zone, *Geophys. J. Int.* **202,** no. 1, 370–380, doi: 10.1093/gji/ggv142.

Bevis, M., K. Hudnut, R. Sanchez, C. Toth, D. Grejner-Brzezinska, E. Kendrick, *et al.* (2005). The B4 project: Scanning the San Andreas and San Jacinto fault zones, *Paper Presented at the AGU Fall Meeting Abstract*, available at https://ui.adsabs.harvard.edu/abs/2005AGUFM.H34B..01B/abstract (last accessed August 2025).

Byrd, R. H., P. Lu, J. Nocedal, and C. Zhu (1995). A limited memory algorithm for bound constrained optimization, *Siam J. Sci. Comput.* **16,** no. 5, 1190–1208, doi: 10.1137/0916069.

Campillo, M., and A. Paul (2003). Long-range correlations in the diffuse seismic coda, *Science* **299,** no. 5606, 547–549, doi: 10.1126/science.1078551.

Capon, J. (1969). High-resolution frequency-wavenumber spectrum analysis, *Proc. IEEE* **57,** no. 8, 1408–1418, doi: 10.1109/PROC.1969.7278.

Chang, J. P., S. A. L. de Ridder, and B. L. Biondi (2016). High-frequency Rayleigh-wave tomography using traffic noise from Long Beach, California, *Geophysics* **81,** no. 2, B43–B53, doi: 10.1190/GEO2015-0415.1.

Chen, J., L. Pan, Z. B. Li, and X. Chen (2022). Continental reworking in the eastern South China block and its adjacent areas revealed by F-J multimodal ambient noise tomography, *J. Geophys. Res.* **127,** no. 11, doi: 10.1029/2022JB024776.

Cheng, F., J. Xia, and C. Xi (2023). Artifacts in high-frequency passive surface wave dispersion imaging: Toward the linear receiver array, *Surv. Geophys.* **44,** no. 4, 1009–1039, doi: 10.1007/s10712-023-09772-1.

Dong, S., Z. Li, X. Chen, and L. Fu (2021). Dispernet: An effective method of extracting and classifying the dispersion curves in the frequency-Bessel dispersion spectrum, *Bull. Seismol. Soc. Am.* **111,** no. 6, 3420–3431, doi: 10.1785/0120210033.

Dor, O., T. K. Rockwell, and Y. Ben-Zion (2006). Geological observations of damage asymmetry in the structure of the San Jacinto, San Andreas and Punchbowl faults in southern California: A possible indicator for preferred rupture propagation direction, *Pure Appl. Geophys.* **163,** no. 2, 301–349, doi: 10.1007/s00024-005-0023-9.

Fu, L., L. Pan, Z. Li, S. Dong, Q. Ma, and X. Chen (2022). Improved high-resolution 3d Vs model of Long Beach, California: Inversion of multimodal dispersion curves from ambient noise of a dense array, *Geophys. Res. Lett.* **49,** no. 4, doi: 10.1029/2021GL097619.

Gabriels, P., R. Snieder, and G. Nolet (1987). Insitu measurements of shear-wave velocity in sediments with higher-mode Rayleigh-waves, *Geophys. Prospect.* **35,** no. 2, 187–196, doi: 10.1111/j.1365-2478.1987.tb00812.x.

Gao, L., W. Zhang, Z. Zhang, and X. Chen (2021). Extraction of multimodal dispersion curves from ambient noise with compressed sensing, *J. Geophys. Res.* **126,** no. 6, doi: 10.1029/2020JB021472.

Hansen, S. M., and B. Schmandt (2015). Automated detection and location of microseismicity at Mount St. Helens with a large-N geophone array, *Geophys. Res. Lett.* **42,** no. 18, 7390–7397, doi: 10.1002/2015GL064848.

Hillers, G., P. Roux, M. Campillo, and Y. Ben-Zion (2016). Focal spot imaging based on zero lag cross-correlation amplitude fields: Application to dense array data at the San Jacinto fault zone, *J. Geophys. Res.* **121,** no. 11, 8048–8067, doi: 10.1002/2016JB013014.

Hu, S., S. Luo, and H. Yao (2020). The frequency-Bessel spectrograms of multicomponent cross-correlation functions from seismic ambient noise, *J. Geophys. Res.* **125,** no. 8, e2020JB019630, doi: 10.1029/2020JB019630.

Lacoss, R. T., E. J. Kelly, and M. N. Toksoz (1969). Estimation of seismic noise structure using arrays, *Geophysics* **34,** no. 1, 21–38, doi: 10.1190/1.1439995.

Li, Z., and X. Chen (2020). An effective method to extract overtones of surface wave from array seismic records of earthquake events, *J. Geophys. Res.* **125,** no. 3, e2019JB018511, doi: 10.1029/2019JB018511.

Li, Z., S. Dong, C. Shi, L. Fu, L. Pan, J. Wang, and X. Chen (2023). Multiple Voronoi partition improves multimodal dispersion imaging from ambient noise: A case study of Lasso dense array, *J. Geophys. Res.* **128,** no. 5, e2022JB026081, doi: 10.1029/2022JB026081.

Li, Z., C. Shi, H. Ren, and X. Chen (2022). Multiple leaking mode dispersion observations and applications from ambient noise cross-correlation in Oklahoma, *Geophys. Res. Lett.* **49,** no. 1, e2021GL096032, doi: 10.1029/2021GL096032.

Li, Z., J. Zhou, G. Wu, J. Wang, G. Zhang, S. Dong, L. Pan, Z. Yang, L. Gao, Q. Ma, *et al.* (2021). Cc-Fjpy: A Python package for extracting overtone surface-wave dispersion from seismic ambient-noise cross correlation, *Seismol. Res. Lett.* **92,** no. 5, 3179–3186, doi: 10.1785/0220210042.

Lin, F.-C., and M. H. Ritzwoller (2011). Helmholtz surface wave tomography for isotropic and azimuthally anisotropic structure, *Geophys. J. Int.* **186,** no. 3, 1104–1120, doi: 10.1111/j.1365-246X.2011.05070.x.

Liu, Y., F. Niu, M. Chen, and W. Yang (2017). 3-D Crustal and uppermost mantle structure beneath Ne China revealed by ambient noise adjoint tomography, *Earth Planet. Sci. Lett.* **461,** 20–29, doi: 10.1016/j.epsl.2016.12.029.

Lu, Y., and Y. Ben-Zion (2022). Validation of seismic velocity models in southern California with full-waveform simulations, *Geophys. J. Int.* **229,** no. 2, 1232–1254, doi: 10.1093/gji/ggab534.

Luo, Y., J. Xia, R. D. Miller, Y. Xu, J. Liu, and Q. Liu (2008). Rayleigh-wave dispersive energy imaging using a high-resolution linear Radon transform, *Pure Appl. Geophys.* **165,** no. 5, 903–922, doi: 10.1007/s00024-008-0338-4.

Ma, Q., L. Pan, J. Wang, Z. Yang, and X. Chen (2022). Crustal S-wave velocity structure beneath the northwestern Bohemian massif, central Europe, revealed by the inversion of multimodal ambient noise dispersion curves, *Front. Earth Sci.* **10,** 838,751, doi: 10.3389/feart.2022.838751.

Maraschini, M., F. Ernst, S. Foti, and L. Socco (2010). A new misfit function for multimodal inversion of surface waves, *Geophysics* **75,** no. 4, G31–G43, doi: 10.1190/1.3436539.

Meng, H., and Y. Ben-Zion (2018). Detection of small earthquakes with dense array data: Example from the San Jacinto fault zone, southern California, *Geophys. J. Int.* **212,** no. 1, 442–457, doi: 10.1093/gji/ggx404.

Mordret, A., M. Landes, N. M. Shapiro, S. C. Singh, and P. Roux (2014). Ambient noise surface wave tomography to determine the shallow shear velocity structure at Valhall: Depth inversion with a neighbourhood algorithm, *Geophys. J. Int.* **198,** no. 3, 1514–1525, doi: 10.1093/gji/ggu217.

Mordret, A., P. Roux, P. Boué, and Y. Ben-Zion (2019). Shallow three-dimensional structure of the San Jacinto fault zone revealed from ambient noise imaging with a dense seismic array, *Geophys. J. Int.* **216,** no. 2, 896–905, doi: 10.1093/gji/ggy464.

Nakata, N., J. P. Chang, J. F. Lawrence, and P. Boue (2015). Body wave extraction and tomography at Long Beach, California, with ambient-noise interferometry, *J. Geophys. Res.* **120,** no. 2, 1159–1173, doi: 10.1002/2015JB011870.

Nolet, G., and G. F. Panza (1976). Array analysis of seismic surface waves: Limits and possibilities, *Pure Appl. Geophys.* **114,** no. 5, 775–790, doi: 10.1007/BF00875787.

Pan, L., X. Chen, J. Wang, Z. Yang, and D. Zhang (2019). Sensitivity analysis of dispersion curves of Rayleigh waves with fundamental and higher modes, *Geophys. J. Int.* **216,** no. 2, 1276–1303, doi: 10.1093/gji/ggy479.

Pan, Y., J. Xia, Y. Xu, Z. Xu, F. Cheng, H. Xu, and L. Gao (2016). Delineating shallow S-wave velocity structure using multiple ambient-noise surface-wave methods: An example from western Junggar, China, *Bull. Seismol. Soc. Am.* **106,** no. 2, 327–336, doi: 10.1785/0120150014.

Park, C. B., and R. D. Miller (2008). Roadside passive multichannel analysis of surface waves (Masw), *J. Environ. Eng. Geophys.* **13,** no. 1, 1–11, doi: 10.2113/JEEG13.1.1.

Qin, L., Y. Ben-Zion, H. Qiu, P. Share, Z. Ross, and F. Vernon (2018). Internal structure of the San Jacinto fault zone in the Trifurcation area southeast of Anza, California, from data of dense seismic arrays, *Geophys. J. Int.* **213,** no. 1, 98–114, doi: 10.1093/gji/ggx540.

Roux, P., L. Moreau, A. Lecointre, G. Hillers, M. Campillo, Y. Ben-Zion, D. Zigone, and F. Vernon (2016). A methodological approach towards high-resolution surface wave imaging of the San Jacinto fault zone using ambient-noise recordings at a spatially dense array, *Geophys. J. Int.* **206,** no. 2, 980–992, doi: 10.1093/gji/ggw193.

Shapiro, N. M., and M. Campillo (2004). Emergence of broadband Rayleigh waves from correlations of the ambient seismic noise, *Geophys. Res. Lett.* **31,** no. 7, doi: 10.1029/2004gl019491.

Shapiro, N. M., and M. H. Ritzwoller (2002). Monte-Carlo inversion for a Global shear-velocity model of the crust and upper mantle, *Geophys. J. Int.* **151,** no. 1, 88–105, doi: 10.1046/j.1365-246X.2002.01742.x.

Shapiro, N. M., M. Campillo, L. Stehly, and M. H. Ritzwoller (2005). High-resolution surface-wave tomography from ambient seismic noise, *Science* **307,** no. 5715, 1615–1618, doi: 10.1126/science.1108339.

Share, P. E., P. Taborik, P. Stepancikova, J. Stemberk, T. K. Rockwell, A. Wade, J. Arrowsmith, A. Donnellan, F. Vernon, and Y. Ben-Zion (2020). Characterizing the uppermost 100 M structure of the San Jacinto fault zone southeast of Anza, California, through joint analysis of geological, topographic, seismic and resistivity data, *Geophys. J. Int.* **222,** no. 2, 781–794, doi: 10.1093/gji/ggaa204.

Song, W., X. Feng, G. Wu, G. Zhang, Y. Liu, and X. Chen (2021). Convolutional neural network, Res-Unet++, -based dispersion curve picking from noise cross-correlations, *J. Geophys. Res.* **126,** no. 11, e2021JB022027, doi: 10.1029/2021JB022027.

Song, W., X. Feng, G. Zhang, L. Gao, B. Yan, and X. Chen (2022). Domain adaptation in automatic picking of phase velocity dispersions based on deep learning. *J. Geophys. Res.* **127,** no. 6, e2021JB023389, doi: 10.1029/2021JB023389.

Tomar, G., E. Stutzmann, A. Mordret, J. P. Montagner, S. C. Singh, and N. M. Shapiro (2018). Joint inversion of the first overtone and fundamental mode for deep imaging at the Valhall oil field using ambient noise, *Geophys. J. Int.* **214,** no. 1, 122–132, doi: 10.1093/gji/ggy122.

Touma, R., T. Blondel, A. Derode, M. Campillo, and A. Aubry (2021). A distortion matrix framework for high-resolution passive seismic 3-D imaging: Application to the San Jacinto fault zone, California, *Geophys. J. Int.* **226,** no. 2, 780–794, doi: 10.1093/gji/ggab133.

Touma, R., A. Aubry, Y. Ben-Zion, and M. Campillo (2022). Distribution of seismic scatterers in the San Jacinto fault zone, southeast of Anza, California, based on passive matrix imaging, *Earth Planet. Sci. Lett.* **578,** 117304, doi: 10.1016/j.epsl.2021.117304.

Trampert, J., and J. H. Woodhouse (1995). Global phase velocity maps of Love and Rayleigh waves between 40 and 150 seconds, *Geophys. J. Int.* **122,** no. 2, 675–690, doi: 10.1111/j.1365-246X.1995.tb07019.x.

U.S. Geological Survey (USGS) (2006). Quaternary Fault and Fold Database for the United States, available at https://earthquake.usgs.gov/hazards/qfaults/ (last accessed January 2017).

Vernon, F., Y. Ben-Zion, and D. Hollis (2014). Sage Brush flats nodal experiment [Dataset], *International Federation of Digital Seismograph Networks. Other/Seismic Network*, doi: 10.7914/SN/ZG_2014.

Wade, A. M. (2018). *Geologic and Structural Characterization of Shallow Seismic Properties Along the San Jacinto Fault at Sage Brush Flat, Southern California (Mscthesis)*, Arizona State University, Arizona.

Wang, G., X. Tian, L. Guo, J. Yan, and Q. Lyu (2018). High-resolution crustal velocity imaging using ambient noise recordings from a high-density seismic array: An example from the Shangrao section of the Xinjiang basin, China, *Earthq. Sci.* **31,** nos. 5/6, 242–251, doi: 10.29382/eqs-2018-0242-4.

Wang, J., G. Wu, and X. Chen (2019). Frequency-Bessel transform method for effective imaging of higher-mode Rayleigh dispersion curves from ambient seismic noise data, *J. Geophys. Res.* **124,** no. 4, 3708–3723, doi: 10.1029/2018JB016595.

Wang, P., J. Chen, X. Feng, L. Pan, and X. Chen (2024). Crust and upper mantle S wave velocity structure in eastern Turkey based on ambient noise tomography, *Tectonophysics* **876,** 230,267, doi: 10.1016/j.tecto.2024.230267.

Wei, Y., X. Tian, Y. Duan, and X. Tian (2018). Imaging the topography of crust-mantle boundary from a high-density seismic array beneath the Middle-Lower Yangtze River, eastern China, *Seismol. Res. Lett.* **89,** no. 5, 1690–1697, doi: 10.1785/0220180045.

Wiggins, R. A. (1972). The general linear inverse problem: Implication of surface waves and free oscillations for earth structure, *Rev. Geophys.* **10,** no. 1, 251–285, doi: 10.1029/RG010i001p00251.

Wu, G., L. Pan, J. Wang, and X. Chen (2020). Shear velocity inversion using multimodal dispersion curves from ambient seismic noise data of Usarray transportable array, *J. Geophys. Res.* **125,** no. 1, e2019JB018213, doi: 10.1029/2019JB018213.

Xi, C., J. Xia, B. Mi, T. Dai, Y. Liu, and L. Ning (2021). Modified frequency-Bessel transform method for dispersion imaging of Rayleigh waves from ambient seismic noise, *Geophys. J. Int.* **225,** no. 2, 1271–1280, doi: 10.1093/gji/ggab008.

Yao, H., R. D. van der Hilst, and M. V. de Hoop (2006). Surface-wave array tomography in Se Tibet from ambient seismic noise and two-station analysis - I. Phase velocity maps, *Geophys. J. Int.* **166,** no. 2, 732–744, doi: 10.1111/j.1365-246X.2006.03028.x.

Yokoi, T. (2010). New formulas derived from seismic interferometry to simulate phase velocity estimates from correlation methods using microtremor, *Geophysics* **75,** no. 4, doi: 10.1190/1.3454210.

Yuan, Y., and X. Chen (2024). Efficient array partitioning method for F-J transform to extract multimode dispersion curves from ambient noise data, *Chin. J. Geophys. (in Chinese)* **67,** no. 2, 492–502, doi: 10.6038/cjg2023R0274.

Zhan, W., L. Pan, and X. Chen (2020). A widespread mid-crustal low-velocity layer beneath northeast China revealed by the multimodal inversion of Rayleigh waves from ambient seismic noise, *J. Asian Earth Sci.* **196,** 104,372, doi: 10.1016/j.jseaes.2020.104372.

Zhang, W., and X. Chen (2006). Traction image method for irregular free surface boundaries in finite difference seismic wave simulation, *Geophys. J. Int.* **167,** no. 1, 337–353, doi: 10.1111/j.1365-246X.2006.03113.x.

Zhang, G. H., Q. Liu, and X. F. Chen (2022). Enhancing the frequency–Bessel spectrogram of ambient noise cross-correlation functions, *Bull. Seismol. Soc. Am.* **113,** no. 1, 361–377, doi: 10.1785/0120220124.

Zhang, W., Z. Zhang, and X. Chen (2012). Three-dimensional elastic wave numerical modelling in the presence of surface topography by a collocated-grid finite-difference method on curvilinear grids, *Geophys. J. Int.* **190,** no. 1, 358–378, doi: 10.1111/j.1365-246X.2012.05472.x.

Zhou, J., and X. Chen (2022). Removal of crossed artifacts from multimodal dispersion curves with modified frequency-Bessel method, *Bull. Seismol. Soc. Am.* **112,** no. 1, 143–152, doi: 10.1785/0120210012.

Zhou, J., Z. Li, and X. Chen (2023). Extending the frequency band of surface-wave dispersion curves by combining ambient noise and earthquake data and self-adaptive normalization, *J. Geophys. Res.* **128,** no. 5, e2022JB026040, doi: 10.1029/2022JB026040.

Manuscript received 30 November 2024
Published online 17 September 2025